

Shadow and Photon Sphere of Black Hole in Clouds of Strings and Quintessence

Aoyun He,^{*} Jun Tao,[†] Yadong Xue,[‡] and Lingkai Zhang[§]

*Center for Theoretical Physics, College of Physics,
Sichuan University, Chengdu, 610065, China*

Abstract

In this work, we study the shadow and photon sphere of the black hole in clouds of strings and quintessence with static and infalling spherical accretions. We obtain the geodesics of the photons near a black hole with different impact parameters b . The string clouds model and quintessence influence the specific intensity by affecting the geodesic and the average radial position of photons. And the range of string clouds parameter a is constrained to ensure that the shadow can be observed. Moreover, we use a model of the photon emissivity $j(\nu_e)$ to get the specific intensities. The light sources in the accretion follow a normal distribution with an attenuation factor γ . The shadow with static spherical accretion is plotted. The apparent shape of the shadow is a perfect circle, and the value of γ affects the brightness of the photon sphere. We investigate the profile and specific intensity of the shadows with static and infalling spherical accretions respectively. The interior of the shadows with an infalling spherical accretion will be darker than that with the static spherical accretion, and the specific intensity with both static and infalling spherical accretion gradually converges.

^{*}Electronic address: heaoyun@stu.scu.edu.cn

[†]Electronic address: taojun@scu.edu.cn

[‡]Electronic address: xueyadong@stu.scu.edu.cn

[§]Electronic address: zhanglingkai@stu.scu.edu.cn

I. INTRODUCTION

The Event Horizon Telescope (EHT) collaboration reported 1.3mm Very Long Baseline Interferometry (VLBI) observations of the nucleus of the nearby galaxy M87, achieving angular resolution comparable to the expected size of the supermassive black hole [1–6]. It promotes the current theoretical study of black hole shadow based on modern astronomical observation methods. The EHT also corroborates that we can directly observe the black hole shadows [7, 8]. Further, the shape of a shadow could be used to study gravity near the event horizon and find whether the general relativity is consistent with the observations [9]. Thus it enables a direct probe of the extreme environment and the dynamics near the black hole.

The shadow of the Schwarzschild black hole was first discussed in [7]. Bardeen [8] soon studied the shadow cast by the Kerr black hole. In recent years, this topic has been extended to other black hole spacetime by various researchers [10–26]. Multiple shadows of a single black hole have also been discussed [27, 28], as well as the shadow of multiple black holes [29]. The black hole shadow in modified GR has also been investigated in [30–33]. The shadows of black hole considering the accretion which can modify the silhouette are studied in [34–36].

The Standard Model of cosmology suggests that dark energy is dominant in our universe [37, 38]. The effect of dark energy on spacetime is similar to the cosmological constant or vacuum energy [39], and the dynamic of dark energy may affect the black hole spacetime [40]. Moreover, modern astronomical observers have found that the universe is in accelerating expansion [41–43], implying a state of negative pressure. Moreover the quintessence dark energy is one of the candidates to interpret the negative pressure. In this model, the state equation of the pressure is $p = \omega_q \rho_q$, where ρ_q is the energy density and ω_q is the state parameter which satisfies $-1 < \omega_q < -1/3$ [44–47]. It is natural to study black hole shadows affected by the quintessence dark energy [40, 48], and the investigation can bring new insights and impose restrictions on the quintessence model. Shadows affected by other dark energy models are also considered in [49, 50].

Theoretical developments propose that the basic unit of nature is one-dimensional strings instead of point-like particles. Studying Einstein’s equations with string clouds may be critical because relativistic strings can be used to construct suitable models [51]. A cloud of strings as the source of the gravitational field was first considered by Latelier [51, 52]. He found an exact solution of Schwarzschild BH surrounded by a cloud of strings. Later, the rotating BHs with a cloud of strings were investigated [53, 54]. Then, the study of a cloud of strings was extended to modified theories of gravity such as Lovelock gravity [55, 56]. Recently, the exact solution of Schwarzschild black hole surrounded by a cloud of strings in Rastall gravity is obtained in [57].

The black hole thermodynamics combined effects of the string clouds and quintessence are considered in [58, 59]. Afterwards, studies in this area were proposed for charged AdS

black hole [60] as well as Lovelock gravity [61]. In this paper, we study the shadow and photon spheres of the black hole surrounded by a cloud of strings and quintessence with both static and infalling spherical accretions. Furthermore, we explore how the photons emissivity $j(\nu_e)$ affects the shadow of the black hole.

This paper is organized as follows. In Section II, we give the metric of a black hole surrounded by quintessence and clouds of strings. Then, we derive the complete null geodesic equations for a photon moving around the static black hole. In addition, the range of parameters affected by string clouds was discussed. In Section III, we study the shadows and photon spheres with static spherical accretions of the uncharged static black hole. In Section IV, the black hole shadows and photon spheres with an infalling spherical accretion are investigated. In Section V, we discuss and conclude our results.

II. METRIC AND PHOTON GEODESIC

The metric of a uncharged static black hole surrounded by quintessence and clouds of strings is given by [58, 59]

$$ds^2 = -f(r)dt^2 + \frac{1}{f(r)}dr^2 + r^2(d\theta^2 + \sin^2\theta d\phi^2), \quad (1)$$

with

$$f(r) = 1 - a - \frac{2M}{r} - \frac{\alpha}{r^{3\omega_q+1}}, \quad (2)$$

where a is the constant affected by the cloud of strings, M is the mass of the black hole, ω_q is the state parameter of quintessence and α is a constant related to the quintessence with density ρ_q as

$$\rho_q = -\frac{\alpha}{2} \frac{3\omega_q}{r^{3(\omega_q+1)}}. \quad (3)$$

The pressure of the quintessence dark energy p should be negative due to the cosmic acceleration. The range of ω_q is $-1 < \omega_q < -1/3$ for $p = \omega_q \rho_q$ [44–47], which causes the existence of event horizon and cosmological horizon. And the region between the two event horizons is called the outer communication domain, for any two observers within it can communicate with each other [62, 63].

Setting $f(r) = 0$ to get two roots, the smaller one is the radius of event horizon r_h and the another is the cosmological horizon r_c . In general it is not easy to get analytic solutions, but for $\omega_q = -2/3$, the analytical solutions of $f(r) = 0$ can be written as

$$r_h = \frac{1 - a + \sqrt{(1 - a)^2 - 8M\alpha}}{2\alpha}, \quad (4)$$

$$r_c = \frac{a - 1 + \sqrt{(1 - a)^2 - 8M\alpha}}{2\alpha}. \quad (5)$$

The values of r_c , r_h corresponding to different ω_q are listed in Table. 1.

Then, we calculate the geodesic of photons to investigate the light deflection with the Euler-Lagrange equation. The Lagrangian takes the form as

$$\mathcal{L} = \frac{1}{2}g_{\mu\nu}\dot{x}^\mu\dot{x}^\nu, \quad (6)$$

where the dot represents the derivative to the affine parameter.

Due to the spherical symmetry of metric, it is convenient to study the photon trajectories on the equatorial plane by setting the initial condition $\theta = \pi/2$ and $\dot{\theta} = 0$. Combine Eqs. (1) and (6) with the Euler-Lagrange equation, we get the equations of time, azimuth, and radial components of the four velocities. Since the metric do not explicitly depend on time t and azimuthal angle ϕ , there are two corresponding conserved quantities as E and L . Then, by redefining the affine parameter λ as $\lambda/|L|$ and using the impact parameter $b = |L|/E$ [64], we get the following equations

$$\dot{t} = \frac{1}{bf(r)}, \quad (7)$$

$$\dot{\phi} = \pm \frac{1}{r^2}, \quad (8)$$

$$\frac{1}{b^2} = \dot{r}^2 + \frac{1}{r^2}f(r), \quad (9)$$

where $+$ and $-$ in Eq. (8) represent the counterclockwise and clockwise direction, respectively for the motion of photons. Moreover, Eq. (9) can be rewritten as

$$\dot{r}^2 + V(r) = \frac{1}{b^2}, \quad (10)$$

where $V(r) = 1/r^2 f(r)$ is the effective potential. At the photon sphere, the photon trajectories satisfy $\dot{r} = 0$ and $\ddot{r} = 0$, which means

$$V(r) = \frac{1}{b^2}, \quad V'(r) = 0. \quad (11)$$

In general, for the radius of photon sphere r_{ph} and corresponding impact parameter b_{ph} , it is not easy to obtain the analytic results. But for $\omega_q = -2/3$, they can be expressed as

$$r_{ph} = \frac{1 - a - \beta}{\alpha}, \quad (12)$$

$$b_{ph} = \sqrt{-\frac{(\beta + a - 1)^3}{\alpha^2(-a(\beta + a - 2) + \beta + 4\alpha M - 1)}}, \quad (13)$$

where

$$\beta = \sqrt{(1 - a)^2 - 6\alpha M}. \quad (14)$$

In order to obtain a realistic solution, there are restrictions $(1 - a)^2 \geq 6\alpha M$ between a and α with $\omega_q = -2/3$. Similar numerical results can be obtained for different ω_q .

The data of r_{ph} , b_{ph} , r_h and r_c is listed in Table. 1 with $\alpha = 0.01$, $M = 1$ and $a = 0.1$. The b_{ph} , r_h and r_c are monotonic while r_{ph} is non-monotonic with the decrease of ω_q . The event horizon radii r_c approaches the cosmological horizon radii r_h with the decrease of ω_q , which leads to a narrower domain of the outer communication. It is worth noting that when $\omega_q = -1/3$, the cosmological horizon radii r_c does not exist, which we use - to denote.

| ω_q | -1/3 | -0.4 | -0.5 | -0.6 | -2/3 | -0.7 | -0.8 | -0.9 | -1 |
|------------|---------|-------------------|---------|---------|---------|---------|---------|---------|---------|
| r_{ph} | 3.37079 | 3.3764 | 3.38524 | 3.39346 | 3.39746 | 3.39860 | 3.39602 | 3.37792 | 3.33333 |
| b_{ph} | 5.37669 | 6.21753 | 6.27757 | 6.36711 | 6.45119 | 6.50322 | 6.71598 | 7.06308 | 7.66965 |
| r_h | 2.04402 | 2.25165 | 2.25997 | 2.27085 | 2.27998 | 2.28525 | 2.30464 | 2.33145 | 2.37016 |
| r_c | - | 5.9×10^9 | 8095.55 | 274.403 | 87.7200 | 57.6865 | 23.1518 | 12.5872 | 8.07703 |

TABLE 1: The data of r_{ph} , b_{ph} , r_h and r_c for different ω_q with $M = 1$, $\alpha = 0.01$ and $a = 0.1$.

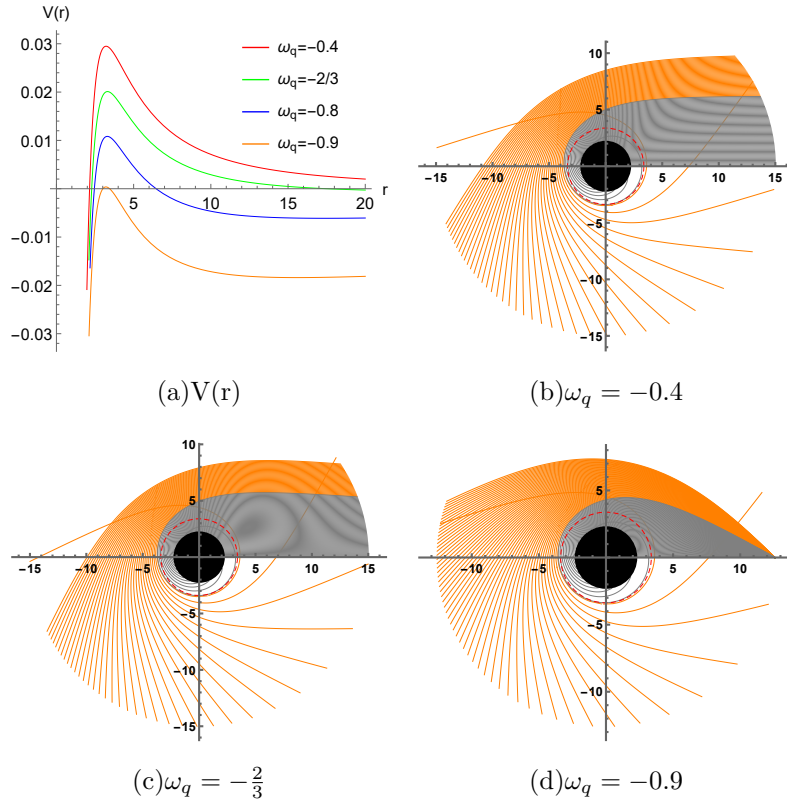


FIG. 1: The effective potential $V(r)$ in FIG. 1(a) and the trajectories of the photons in other images for different ω_q with $\alpha = 0.01$ and $a = 0.1$.

The Eq. (10) shows that the null geodesic depends on the impact parameter b and the effective potential $V(r)$. The effective potential for different ω_q is plotted in FIG. 1(a). The

effective potential vanishes at the event horizon, increases and reaches a maximum at the photon sphere, finally vanishes at the cosmological horizon.

The geodesics of photons can be plotted by the equation of motion. Combining Eqs. (8) and (9), we have

$$\frac{dr}{d\phi} = \pm r^2 \sqrt{\frac{1}{b^2} - \frac{1}{r^2} f(r)} \equiv \Phi(r). \quad (15)$$

For a photon that is approaching the black hole, it either escapes or falls into the black hole. When $b > b_{ph}$, it escapes and its trajectory have a nearest radial position which is set as r_i . The turning point r_i can be gotten from the equation $\Phi(r) = 0$. The radial position r_i is important to obtain the photons trajectory, it can also be the lower integral limit in the backward ray shooting method [65]. For $b < b_{ph}$, the photons trajectories would not have r_i because the photon will continue to approach the black hole and finally falls into it. To get the trajectories of the photons, the location of the observer is also important. Physically, the observer is located near the cosmological horizon in the outer domain of communication. In other words it will start from a position near r_c .

Setting the starting point of the photons trajectories on the x-axis close to r_c and our plot range to be $r \leq 15$, the trajectories of photons are plotted in FIG. 1 for different quintessence state parameter ω_q with $a = 0.1$ and $\alpha = 0.01$ according to Eq. (15) and the analysis above.

The quintessence state parameter ω_q will impact the location of the starting point and the curvature of geodesics. The values of r_c for different ω_q are listed in Table. 1. For $\omega_q = -0.4$ in FIG. 1(b), the geodesics are near-parallel because the value of r_c is much larger than our plot range ($r_c = 5.9 \times 10^9$). Since the cosmological horizon $r_c = 12.5872$ from Table. 1 when $\omega_q = -0.9$, the plot range should be $r \leq r_c$ in FIG. 1(d). The geodesics here are more curved since the value of r_c is close to the radius of cosmological horizon r_h ($r_h = 2.33145$).

For the geodesics in FIG. 1, the orange and gray lines represent the geodesics of photons starts from $b > b_{ph}$ and $b < b_{ph}$ respectively. It is worth noting that when $b = b_{ph}$, the photons will continue to rotate around the black hole in an unstable circular orbit [66] located at r_{ph} , which is also known as the photon sphere [67] and the red dashed line represents the photon sphere and the black disk represents the black hole.

Next, we study the geodesics for different a with fixed ω_q and α . The values of r_{ph} , b_{ph} , r_h and r_c are also listed in Table. 2 for the following analysis. Using the same method, we set $\omega_q = -2/3$ and $\alpha = 0.01$ to study geodesics under the influence of the string clouds by calculating the values of various radius and get the trajectories of photons under different a .

From Table. 2, the r_{ph} , b_{ph} , r_h and r_c all vary monotonically with a . The geodesics with different a are drawn in FIG. 2 either. According to the value of r_c in Table. 2, the same conclusion can be obtained as in the above analysis. In FIG. 2(d), the plot range is $r \leq r_c$ ($r_c = 34.1421$). it can be seen that the deflection angle of the photons increases with increasing a .

| a | 0 | 0.1 | 0.2 | 0.3 | 0.4 | 0.5 | 0.6 |
|----------|---------|---------|---------|---------|---------|---------|---------|
| r_{ph} | 3.04640 | 3.39746 | 3.84227 | 4.42561 | 5.22774 | 6.41101 | 8.37722 |
| b_{ph} | 5.44501 | 6.45119 | 7.82587 | 9.80258 | 12.864 | 18.2114 | 30.0948 |
| r_h | 2.04168 | 2.27998 | 2.58343 | 2.98438 | 3.54249 | 4.38447 | 5.85786 |
| r_c | 97.9583 | 87.7200 | 77.4166 | 67.0156 | 56.4575 | 45.6155 | 34.1421 |

TABLE 2: The values of r_{ph} , b_{ph} , r_h and r_c for different a with $\omega_q = -2/3$ and $\alpha = 0.01$.

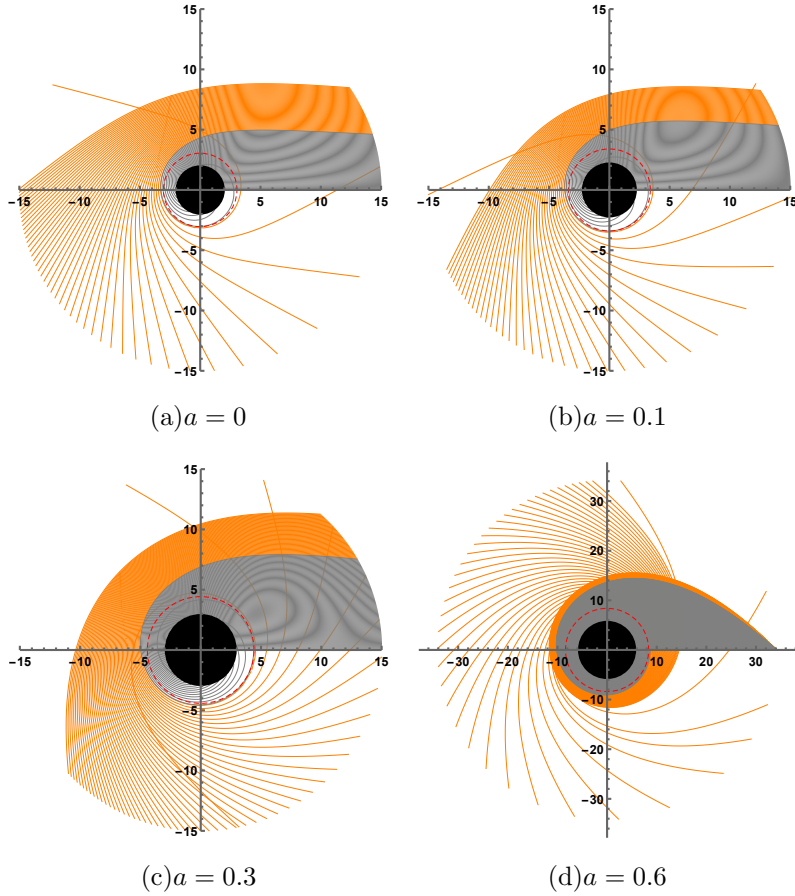


FIG. 2: The trajectory of the photons for different a with $\omega_q = -2/3$ and $\alpha = 0.01$.

The range of a is not arbitrary, it should be noted that the cosmological horizon r_c must be larger than the black hole horizon r_h to ensure that the outer communication domain exists. With the increase of a , the distance between r_c and b_{ph} becomes small, which suggests the parameter a has an upper limit $a_m = a_m(\omega_q)$ to have $r_c > b_{ph}$. For example, when $\omega_q = -2/3$ and $\alpha = 0.01$, we get $a < 0.612158$.

III. SHADOWS AND PHOTON SPHERES WITH STATIC SPHERICAL ACCRETIONS

In this section, we study the effect of accretion profile on black hole shadows and take spherical accretion as an example. Based on the backward ray shooting method [65] we focus on the specific intensity observed by the static observer [68, 69]. The photons emissivity can be expressed as

$$j(\nu_e) \propto \rho(r)P(\nu_e), \quad (16)$$

where $\rho(r)$ is the density of light sources in the accretion and P represent the probability about spectral distribution. For the spherical accretions, the density of light sources follows a normal distribution and can be expressed as

$$\rho(r) = \sqrt{\frac{\gamma}{\pi}} e^{-\gamma r^2}, \quad (17)$$

where γ is the coefficient to control the decay rate and $\sqrt{\gamma/\pi}$ is the normalization factor.

The light emitted by the source in the accretion is not strictly monochromatic, which obeys a Gaussian distribution [65]. We assume the central frequency is ν_* and its width is $\Delta\nu$, while the effect of photons outside the spectral width is neglected in this paper. Then the probability P that the frequency of light is located at the spectrum width can be written as

$$P(\nu_e) = \int_{\nu_* - \Delta\nu}^{\nu_* + \Delta\nu} \frac{1}{\Delta\nu\sqrt{\pi}} e^{-\frac{(\nu - \nu_*)^2}{\Delta\nu^2}} d\nu, \quad (18)$$

where $1/\Delta\nu\sqrt{\pi}$ is the normalization factor. Combining Eqs. (16), (17) and (18), we can express photons emissivity in the rest-frame of the emitter as

$$j(\nu_e) \propto \int_{\nu_* - \Delta\nu}^{\nu_* + \Delta\nu} \frac{\sqrt{\gamma}}{\pi\Delta\nu} e^{-\frac{(\nu - \nu_*)^2}{\Delta\nu^2} - \gamma r^2} d\nu. \quad (19)$$

The specific intensity received by a distant observer is given as an integral along the null geodesic [65], and can be expressed as

$$I(b) = \int_{ray} \frac{\nu_o^3}{\nu_e^3} j(\nu_e) dl_{prop} = \int_{ray} g^3 j(\nu_e) dl_{prop}, \quad (20)$$

where ν_o is the frequency observed and dl_{prop} is the proper length as measured in the frame comoving with acceleration, the ratio of ν_o and ν_e is the redshift factor g . For a static spherically symmetric black hole, we have $g = \sqrt{f(r)}$. And in this spacetime, we can easily obtain

$$dl_{prop} = \pm \sqrt{f(r)^{-1} + r^2 \left(\frac{d\phi}{dr}\right)^2} dr, \quad (21)$$

where $+$ and $-$ correspond to the case that the photons approach and leave the black hole respectively.

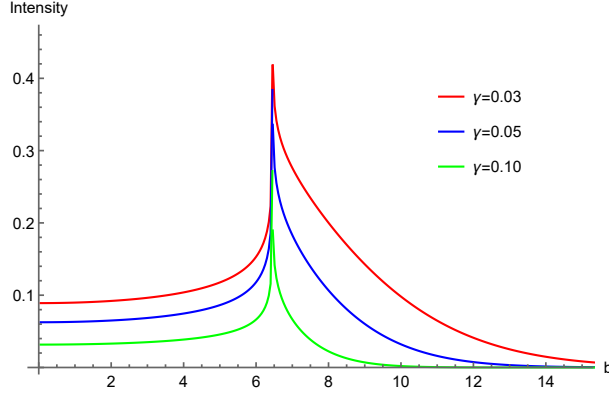


FIG. 3: The specific intensity with static spherical accretion for different γ with $\omega_q = -2/3$, $a = 0.1$ and $\alpha = 0.01$.

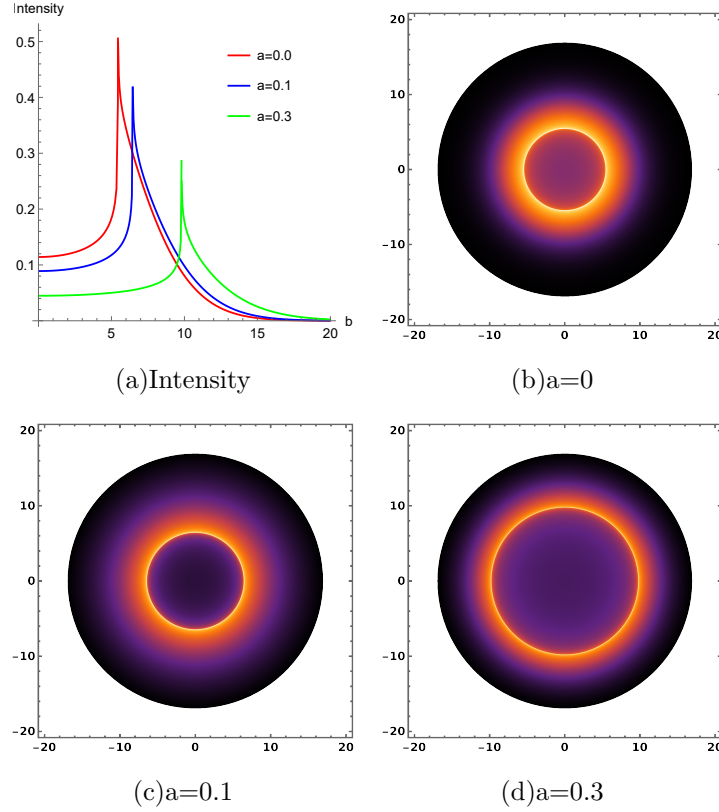


FIG. 4: The specific intensity for different a in FIG. 4(a) and the black hole shadow with static spherical accretion for different a in other images with $\omega_q = -2/3$ and $\alpha = 0.01$.

Combining the Eqs. (19), (20) and (21), we can get the specific intensity $I(b)$ with impact

parameter b . Then use it to investigate different coefficient γ with static spherical accretion in Fig. 3. The coefficient γ affects the intensity's decay rate. As b increases, the intensity ramps up first when $b < b_{ph}$, then reaches a peak at b_{ph} , finally drops rapidly to smaller values. For $b = b_{ph}$, the photon revolves around the black hole several times, causing the observed intensity to be maximal. However, due to the limitation of calculation accuracy and the logarithmic form of the intensity, the actual calculated intensity will never reach infinity [67]. For $b > b_{ph}$, the density of light sources in the accretion goes small, then the observed intensity vanishes for large enough b . So the coefficient γ does not impact the intrinsic properties of spacetime geometry, which means the peak of the specific intensity is always located at $b = b_{ph}$. For convenience, the images of specific intensity below are all fixed with $\gamma = 0.03$.

The observed specific intensities and shadows for different parameter a are plotted in FIG. 4 with $\omega_q = -2/3$ and $\alpha = 0.01$. For the specific intensity in FIG. 4(a), the string clouds parameter a affects the maximum value of specific intensity and the radius of the photon spheres, which is consistent with the analysis in Table. 2. As the parameter a increases, the radii of the cosmological horizon r_c gets small rapidly which causes the upper limit of the integration gets small. Moreover, the lower limit of the integration r_h also gets large, albeit slowly. The result is that the geodesics of photons become short rapidly with a increasing which causes the average specific intensity gets smaller.

FIG. 4(b), (c) and (d) show the black hole shadows for different parameter a in the region $b \leq 17$. Different colors correspond to different values of the specific intensity, and all profiles of the shadows use one color function in which the greater specific intensity means the brighter, while the smaller means the darker. We can directly compare the intensity magnitude inside and outside the photon sphere. The shadow is circularly symmetric, and the photon sphere is a bright ring outside the black hole.

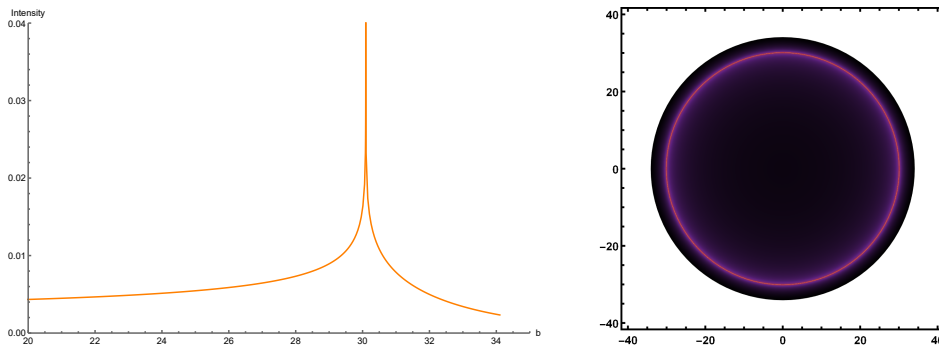


FIG. 5: The specific intensity and the black hole shadow with static spherical accretion for $a = 0.6$, $\omega_q = -2/3$ and $\alpha = 0.01$.

As the parameter a of string clouds converges to a maximum value, the radius of shadow

approaches the cosmological horizon. When $\omega_q = -2/3$ and $\alpha = 0.01$, we get $a < 0.612158$. From the Table. 2, we can see that $r_c = 34.1421$ and $b_{ph} = 30.0948$ when $a = 0.6$. The observed specific intensity and shadow for $a = 0.6$ is drawn in Fig. 5. Most of the specific intensity is concentrated around $b = b_{ph}$ in Fig. 5(a). Moreover, from the profile of shadow in Fig. 5(b), it can be observed that all regions are relatively dark except for the vicinity of $b = b_{ph}$.

Using the same method, we investigated the specific intensities and the shadows for different ω_q with $a = 0.1$ and $\alpha = 0.01$ in FIG. 6. From the image of specific intensity in FIG. 6(a), it can be seen that ω_q would also affect the maximum value of specific intensity and the radius of the photon spheres. As ω_q decreases, the radius of the shadow increases. It can be seen from Table. 1 that $r_c = 12.5872$ and $b_{ph} = 7.06308$ for $\omega_q = -0.9$ which is smaller than the region of the images so we especially set the region in FIG. 6(d) to be $b \leq r_c$. The specific intensity inside the photon sphere does not vanish but has a small finite value. This is because some photons near the black hole have escaped [49, 64].

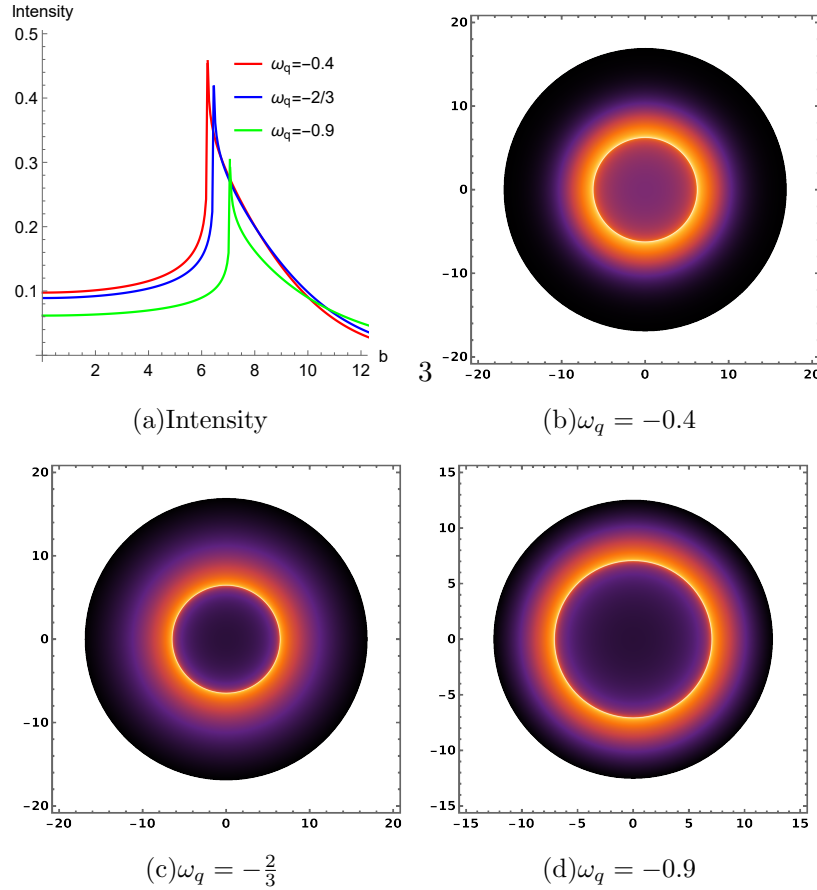


FIG. 6: The specific intensity for different ω_q in FIG. 6(a) and the black hole shadow with static spherical accretion for different ω_q in other images with $a = 0.1$ and $\alpha = 0.01$.

IV. SHADOWS AND PHOTON SPHERES WITH AN INFALLING SPHERICAL ACCRETION

In this section, the accreting matter is free-falling in a static and spherically symmetric spacetime. When the angular velocity of the black hole is not considered, the accretion matter will only have radial velocity towards the black hole. We still employ Eq. (20) to investigate the shadow. The redshift factor in this model can be written as

$$g = \frac{p_\alpha u_o^\alpha}{p_\beta u_e^\beta}, \quad (22)$$

where p_μ is the 4-momentum of photons, $u_o^\mu = (1, 0, 0, 0)$ is the 4-velocity of the distant observer, and u_e^μ is the 4-velocity of the photons emitted from the accretion. Obviously, the matter which emits the photons at different locations has different radial velocities due to tidal forces from the black hole. In the infalling accretion, the u_e^μ can be expressed as [68]

$$u_e^t = \frac{1}{A(r)}, \quad u_e^r = -\sqrt{\frac{1-A(r)}{A(r)B(r)}}, \quad u_e^\theta = u_e^\phi = 0. \quad (23)$$

From Eq. (1), we simply set $A(r) = f(r)$, $B(r) = 1/f(r)$ [64]. As p_t is a constant and $p_\alpha p^\alpha = 0$, we can get

$$p_r = \pm p_t \sqrt{\frac{1}{f(r)} \left(\frac{1}{f(r)} - \frac{b^2}{r^2} \right)}. \quad (24)$$

Combining Eqs. (22), (23) and (24), the redshift factor can be expressed as

$$g = -\frac{f(r)}{\sqrt{1-f(r)} \sqrt{1 - \frac{b^2 f(r)}{r^2}} - 1}. \quad (25)$$

Substituting Eqs. (19), (21) and (25) into Eq. (20) to get a function of specific intensity that are determined by the impact parameter b , then we can plot the black hole shadows with an infalling spherical accretion. The shadows for $a = 0.1$ and $a = 0.3$ are drawn in Fig. 7(b) and Fig. 7(c) respectively with $\omega_q = -2/3$ and $\alpha = 0.01$. The interior of the shadows with an infalling spherical accretion will be darker than that with the static spherical accretion. Due to the radial velocity of the accreting matter, the frequency of the photons we received is reduced and the profile of shadow is darker. The same conclusion can be shown from Eq.(25).

We are also interested in the difference for the specific intensity between static and infalling spherical accretion. With $\omega_q = -2/3$ and $\alpha = 0.01$, we plot the graph of specific intensity with static and infalling spherical accretion for $a = 0.1$ and $a = 0.3$ in Fig. 7(a)

and Fig. 7(c) respectively. As analyzed above, the blue line is much lower than the red line in $b < b_{ph}$. with b increasing, the specific intensity I with either static or infalling spherical accretion gradually converge, because the emitted photon with larger impact parameter b will have a smaller average radial component in the integral along the trajectory, and the effect of the redshift factor becomes smaller. When $a = 0.3$ in Fig. 7(c), the difference between the blue line and the red line also becomes larger since the observers and black holes get closer, which in turn leads to a larger redshift factor g from Eq.(25).

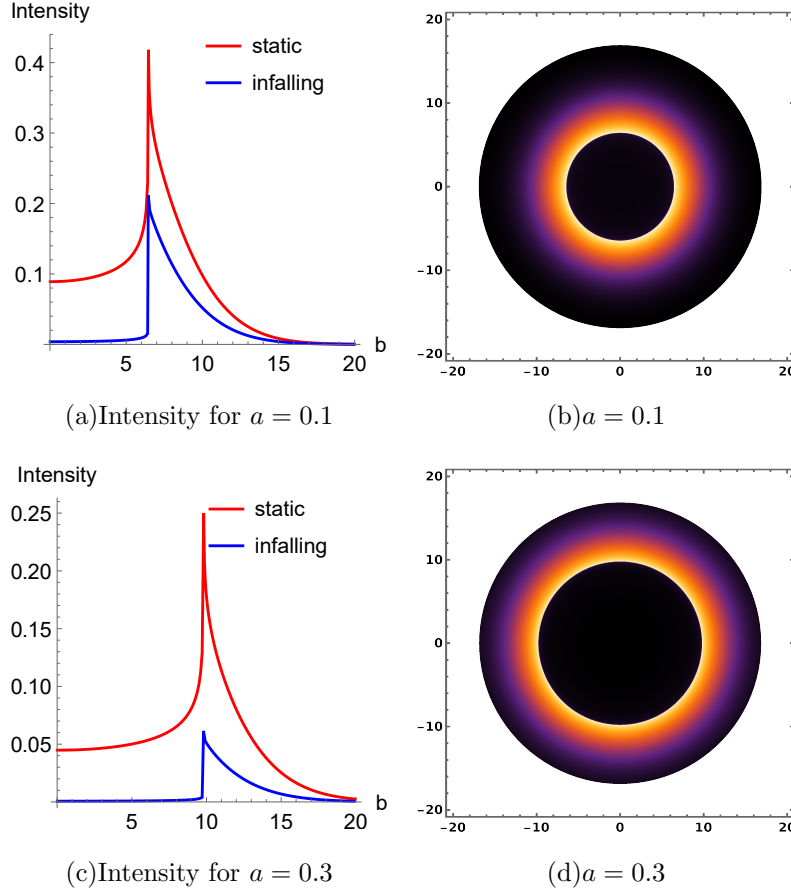


FIG. 7: The specific intensity with static and infalling spherical accretion for $a = 0.1$ and $a = 0.3$ in FIG. 7(a) and FIG. 7(c) respectively. And the profile of black hole shadows with an infalling spherical accretion for $a = 0.1$ and $a = 0.3$ in FIG. 7(b) and 7(d) respectively with $\omega_q = -2/3$ and $\alpha = 0.01$.

In the same way, we further investigate how different ω_q impact the specific intensity with an infalling spherical accretion in Fig. 8. From Table. 1, the radius of shadow b_{ph} varies very slowly with ω_q , which causes the bright rings in Fig. 8(b) and Fig. 8(d) to have similar sizes. For both static and infalling spherical accretion, the specific intensity varies for different ω_q because the length of the optics path varies with ω_q .

Either with static or infalling spherical accretion, the shadow have an equal radii in FIG.

7(a) and (c), in other words, the peak of the images of specific intensity are all located at $b = b_{ph}$. We can conclude that the model of the accretion we considered in this paper only affects the value of the specific intensity but not the profile. Because the radius of the shadow and photon sphere is actually the intrinsic properties of spacetime.

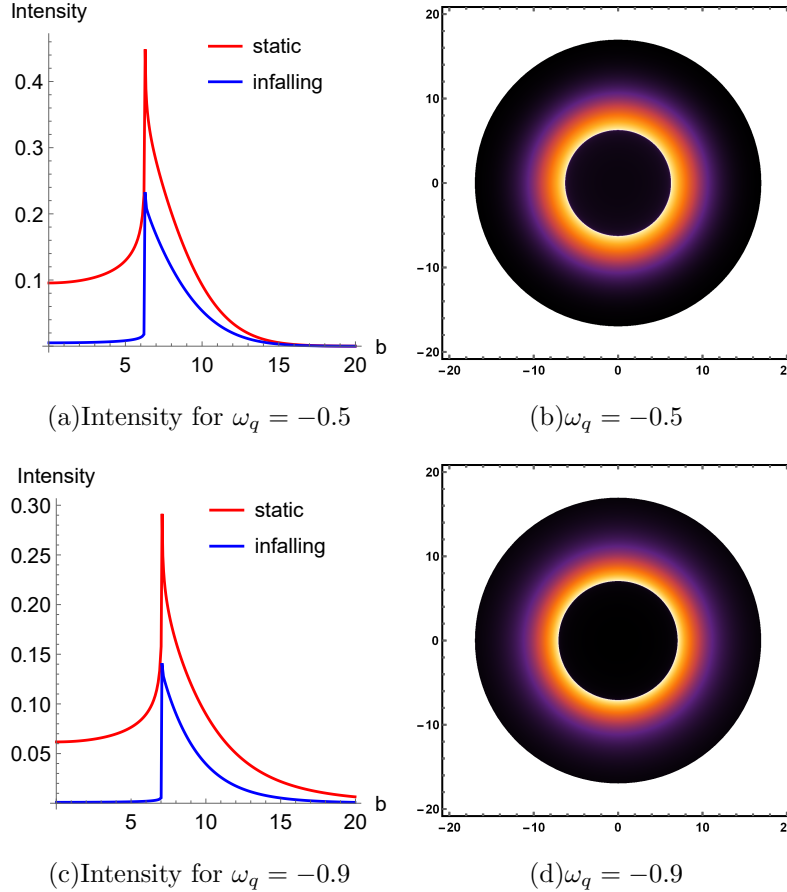


FIG. 8: The specific intensity with static and infalling spherical accretion in FIG. 8(a) and FIG. 8(c) and the profile of black hole shadows with an infalling spherical accretion in FIG. 8(b) and 8(d) for $\omega_q = -0.5$ and $\omega_q = -0.9$ respectively with $a = 0.1$ and $\alpha = 0.01$.

V. CONCLUSION AND DISCUSSION

We firstly derived the black hole solution combining quintessence and string clouds, and used the Euler-Lagrangian equation to get the geodesics of photons. By analyzing the influence of parameters on photons trajectories, we learn that the radius of the photon sphere r_{ph} is non-monotonic with ω_q decreasing, which is consistent with the previous results [49]. When a increases, the radius of the event horizon r_h , cosmological horizon r_c , photon sphere r_{ph} , the corresponding impact parameter b_{ph} are all monotonic. Next, we discussed the range of a in different ω_q . As the photons are deflected, it forms the shadow of a black

hole.

Moreover, we studied the black hole shadow with static and infalling spherical accretions respectively. The backward ray shooting method helps us obtained the specific intensity $I(b)$ from a static observer. For the spherical accretion, we guess the density of light sources follows a normal distribution affected by the coefficient γ and the light emitted is not strictly monochromatic. Moreover, its frequencies conform to the Gaussian distribution with a central frequency ν_* and width $\Delta\nu$. The photon emissivity is written as $j(\nu_e)$. Using the backward ray shooting method and the model of the photon emissivity, we plotted the shadow and photon sphere with static and infalling spherical accretions. Due to the Doppler effect, the interior of the shadow with an infalling spherical accretion will be darker. Different ω_q and a would change the size and intensity of the shadow. We investigated the specific emissivity with different coefficients γ and found that the intensity will decrease as γ increases.

In the presence of the cosmological horizon, the range of a is not arbitrary, but need to satisfy $r_c > b_{ph}$. Because if $r_c < b_{ph}$, then all photons emitted from the observer will not be able to escape from the black hole, which caused the specific intensity to be little.

Actually, the backward ray shooting method has some flaws that when we compare the specific intensity observed by observers at different distances from the black hole, the intensity observed by the distant observer is stronger than that of the close observer in Fig. 6(a) and Fig. 4(a). When the cosmological horizon is not considered, in other words, when the observer's position is fixed, the ray shooting method may appear more realistic. We can also make it appear more realistic in a different way even when the observer's position changes with the size of cosmological horizon r_c , such as improving the accretion model or using a more realistic frequency distribution function.

The EHT Collaboration portrays M87* and claims that the observation supports General Relativity. We expect this to bring insights and implications for the quintessence dark energy model and the string theory from the observations of the shadow images of the black holes in future astronomical observation projects.

Acknowledgments

We are grateful to Peng Wang, Hanwen Feng, Yuchen Huang, Qingyu Gan and Wei Hong for useful discussions. This work is supported by NSFC (Grant No.11947408 and 12047573).

-
- [1] K. Akiyama *et al.* [Event Horizon Telescope], First M87 Event Horizon Telescope Results. I. The Shadow of the Supermassive Black Hole, *Astrophys. J. Lett.* **875**, L1 (2019).
 - [2] K. Akiyama *et al.* [Event Horizon Telescope], First M87 Event Horizon Telescope Results. II. Array and Instrumentation, *Astrophys. J. Lett.* **875**, no.1, L2 (2019).

- [3] K. Akiyama *et al.* [Event Horizon Telescope], First M87 Event Horizon Telescope Results. III. Data Processing and Calibration, *Astrophys. J. Lett.* **875**, no.1, L3 (2019).
- [4] K. Akiyama *et al.* [Event Horizon Telescope], First M87 Event Horizon Telescope Results. IV. Imaging the Central Supermassive Black Hole, *Astrophys. J. Lett.* **875**, no.1, L4 (2019).
- [5] K. Akiyama *et al.* [Event Horizon Telescope], First M87 Event Horizon Telescope Results. V. Physical Origin of the Asymmetric Ring, *Astrophys. J. Lett.* **875**, no.1, L5 (2019).
- [6] K. Akiyama *et al.* [Event Horizon Telescope], First M87 Event Horizon Telescope Results. VI. The Shadow and Mass of the Central Black Hole, *Astrophys. J. Lett.* **875**, no.1, L6 (2019).
- [7] J. L. Synge, The Escape of Photons from Gravitationally Intense Stars, *Mon. Not. Roy. Astron. Soc.* **131**, no.3, 463-466 (1966).
- [8] J. M. Bardeen, W. H. Press and S. A. Teukolsky, chrotron radiation, *Astrophys. J.* **178**, 347 (1972).
- [9] Y. Mizuno, Z. Younsi, C. M. Fromm, O. Porth, M. De Laurentis, H. Olivares, H. Falcke, M. Kramer and L. Rezzolla, The Current Ability to Test Theories of Gravity with Black Hole Shadows, *Nature Astron.* **2**, no.7, 585-590 (2018).
- [10] K. Hioki and K. i. Maeda, Measurement of the Kerr Spin Parameter by Observation of a Compact Object's Shadow, *Phys. Rev. D* **80**, 024042 (2009).
- [11] N. Tsukamoto, Black hole shadow in an asymptotically-flat, stationary, and axisymmetric spacetime: The Kerr-Newman and rotating regular black holes, *Phys. Rev. D* **97**, no.6, 064021 (2018).
- [12] R. Takahashi, Black hole shadows of charged spinning black holes, *Publ. Astron. Soc. Jap.* **57**, 273 (2005).
- [13] Q. Gan, P. Wang, H. Wu and H. Yang, Photon ring and observational appearance of a hairy black hole, *Phys. Rev. D* **104** (2021) no.4, 044049.
- [14] S. W. Wei and Y. X. Liu, Observing the shadow of Einstein-Maxwell-Dilaton-Axion black hole, *JCAP* **11**, 063 (2013).
- [15] A. Abdujabbarov, F. Atamurotov, Y. Kucukakca, B. Ahmedov and U. Camci, Shadow of Kerr-Taub-NUT black hole, *Astrophys. Space Sci.* **344**, 429-435 (2013).
- [16] J. Podolsky and R. Svarc, Interpreting spacetimes of any dimension using geodesic deviation, *Phys. Rev. D* **85**, 044057 (2012).
- [17] J. Schee and Z. Stuchlik, Optical phenomena in the field of braneworld Kerr black holes, *Int. J. Mod. Phys. D* **18**, 983-1024 (2009).
- [18] C. Bambi, F. Caravelli and L. Modesto, Direct imaging rapidly-rotating non-Kerr black holes, *Phys. Lett. B* **711**, 10-14 (2012).
- [19] C. Bambi and N. Yoshida, Shape and position of the shadow in the $\delta = 2$ Tomimatsu-Sato space-time, *Class. Quant. Grav.* **27**, 205006 (2010).
- [20] Z. Younsi, A. Zhidenko, L. Rezzolla, R. Konoplya and Y. Mizuno, New method for shadow calculations: Application to parametrized axisymmetric black holes, *Phys. Rev. D* **94**, no.8,

- 084025 (2016).
- [21] P. V. P. Cunha, C. A. R. Herdeiro, B. Kleihaus, J. Kunz and E. Radu, Shadows of Einstein–dilaton–Gauss–Bonnet black holes, *Phys. Lett. B* **768**, 373-379 (2017).
 - [22] S. Dastan, R. Saffari and S. Soroushfar, Shadow of a Kerr-Sen dilaton-axion Black Hole, [arXiv:1610.09477 [gr-qc]].
 - [23] A. Abdujabbarov, M. Amir, B. Ahmedov and S. G. Ghosh, Shadow of rotating regular black holes, *Phys. Rev. D* **93**, no.10, 104004 (2016).
 - [24] M. Amir and S. G. Ghosh, Shapes of rotating nonsingular black hole shadows, *Phys. Rev. D* **94**, no.2, 024054 (2016).
 - [25] A. Saha, S. M. Modumudi and S. Gangopadhyay, Shadow of a noncommutative geometry inspired Ayón Beato García black hole, *Gen. Rel. Grav.* **50**, no.8, 103 (2018).
 - [26] E. F. Eiroa and C. M. Sendra, Shadow cast by rotating braneworld black holes with a cosmological constant, *Eur. Phys. J. C* **78**, no.2, 91 (2018).
 - [27] P. V. P. Cunha, C. A. R. Herdeiro, E. Radu and H. F. Runarsson, Shadows of Kerr black holes with scalar hair, *Phys. Rev. Lett.* **115**, no.21, 211102 (2015).
 - [28] J. Grover, J. Kunz, P. Nedkova, A. Wittig and S. Yazadjiev, Multiple shadows from distorted static black holes, *Phys. Rev. D* **97**, no.8, 084024 (2018).
 - [29] A. Yumoto, D. Nitta, T. Chiba and N. Sugiyama, Shadows of Multi-Black Holes: Analytic Exploration, *Phys. Rev. D* **86**, 103001 (2012).
 - [30] L. Amarilla, E. F. Eiroa and G. Giribet, Null geodesics and shadow of a rotating black hole in extended Chern-Simons modified gravity, *Phys. Rev. D* **81**, 124045 (2010).
 - [31] R. Kumar, B. P. Singh, M. S. Ali and S. G. Ghosh, Rotating black hole shadow in Rastall theory, [arXiv:1712.09793 [gr-qc]].
 - [32] T. Vetsov, G. Gyulchev and S. Yazadjiev, Shadows of Black Holes in Vector-Tensor Galileons Modified Gravity, [arXiv:1801.04592 [gr-qc]].
 - [33] J. R. Mureika and G. U. Varieschi, Black hole shadows in fourth-order conformal Weyl gravity, *Can. J. Phys.* **95**, no.12, 1299-1306 (2017).
 - [34] V. Perlick and O. Y. Tsupko, Light propagation in a plasma on Kerr spacetime: Separation of the Hamilton-Jacobi equation and calculation of the shadow, *Phys. Rev. D* **95**, no.10, 104003 (2017).
 - [35] P. V. P. Cunha and C. A. R. Herdeiro, Shadows and strong gravitational lensing: a brief review, *Gen. Rel. Grav.* **50**, no.4, 42 (2018).
 - [36] R. A. Konoplya, Shadow of a black hole surrounded by dark matter, *Phys. Lett. B* **795**, 1-6 (2019).
 - [37] A. C. Pope *et al.* [SDSS], Cosmological parameters from Eigenmode analysis of Sloan Digital Sky Survey galaxy redshifts, *Astrophys. J.* **607**, 655-660 (2004).
 - [38] E. Komatsu *et al.* [WMAP], Seven-Year Wilkinson Microwave Anisotropy Probe (WMAP) Observations: Cosmological Interpretation, *Astrophys. J. Suppl.* **192**, 18 (2011).

- [39] E. J. Copeland, M. Sami and S. Tsujikawa, Dynamics of dark energy, *Int. J. Mod. Phys. D* **15**, 1753-1936 (2006).
- [40] V. V. Kiselev, Quintessence and black holes, *Class. Quant. Grav.* **20**, 1187-1198 (2003).
- [41] S. Perlmutter *et al.* [Supernova Cosmology Project], Measurements of Ω and Λ from 42 high redshift supernovae, *Astrophys. J.* **517**, 565-586 (1999).
- [42] A. G. Riess *et al.* [Supernova Search Team], Observational evidence from supernovae for an accelerating universe and a cosmological constant, *Astron. J.* **116**, 1009-1038 (1998).
- [43] P. M. Garnavich *et al.* [Supernova Search Team], Supernova limits on the cosmic equation of state, *Astrophys. J.* **509**, 74-79 (1998).
- [44] B. Stern, Y. Tikhomirova, M. Stepanov, D. Kompaneets, A. Berezhnoy and R. Svensson, Search for non-triggered gamma-ray bursts in the batse continuous records: preliminary results, *Astrophys. J. Lett.* **540**, L21 (2000).
- [45] N. A. Bahcall, J. P. Ostriker, S. Perlmutter and P. J. Steinhardt, The Cosmic triangle: Assessing the state of the universe, *Science* **284**, 1481-1488 (1999).
- [46] P. J. Steinhardt, L. M. Wang and I. Zlatev, Cosmological tracking solutions, *Phys. Rev. D* **59**, 123504 (1999).
- [47] L. M. Wang, R. R. Caldwell, J. P. Ostriker and P. J. Steinhardt, Cosmic concordance and quintessence, *Astrophys. J.* **530**, 17-35 (2000).
- [48] V. Sahni, Cosmological surprises from braneworld models of dark energy, [arXiv:astro-ph/0502032 [astro-ph]].
- [49] X. X. Zeng and H. Q. Zhang, Influence of quintessence dark energy on the shadow of black hole, *Eur. Phys. J. C* **80**, no.11, 1058 (2020).
- [50] S. U. Khan and J. Ren, Shadow cast by a rotating charged black hole in quintessential dark energy, *Phys. Dark Univ.* **30**, 100644 (2020).
- [51] P. S. Letelier, Clouds of Strings in general relativity, *Phys. Rev. D* **20**, 1294-1302 (1979).
- [52] P. S. Letelier, String cosmologies, *Phys. Rev. D* **28**, 2414-2419 (1983).
- [53] D. Barbosa and V. B. Bezerra, On the rotating Letelier spacetime, *Gen. Rel. Grav.* **48**, no.11, 149 (2016).
- [54] J. M. Toledo and V. B. Bezerra, Kerr–Newman–AdS black hole with quintessence and cloud of strings, *Gen. Rel. Grav.* **52**, no.4, 34 (2020).
- [55] E. Herscovich and M. G. Richarte, Black holes in Einstein-Gauss-Bonnet gravity with a string cloud background, *Phys. Lett. B* **689**, 192-200 (2010).
- [56] J. M. Toledo and V. B. Bezerra, Black holes with a cloud of strings in pure Lovelock gravity, *Eur. Phys. J. C* **79**, no.2, 117 (2019).
- [57] X. C. Cai and Y. G. Miao, Quasinormal modes and spectroscopy of a Schwarzschild black hole surrounded by a cloud of strings in Rastall gravity, *Phys. Rev. D* **101**, no.10, 104023 (2020).
- [58] Y. Ma, Y. Zhang, R. Zhao, S. Cao, T. Liu, S. Geng, Y. Liu and Y. Huang, Phase transitions and entropy force of charged de Sitter black holes with cloud of string and quintessence,

- [arXiv:1907.11870 [hep-th]].
- [59] M. Chabab and S. Iraoui, Thermodynamic criticality of d-dimensional charged AdS black holes surrounded by quintessence with a cloud of strings background, *Gen. Rel. Grav.* **52**, no.8, 75 (2020).
 - [60] J. M. Toledo and V. B. Bezerra, Some remarks on the thermodynamics of charged AdS black holes with cloud of strings and quintessence, *Eur. Phys. J. C* **79**, no.2, 110 (2019).
 - [61] J. de M. Toledo and V. B. Bezerra, Black holes with cloud of strings and quintessence in Lovelock gravity, *Eur. Phys. J. C* **78**, no.7, 534 (2018).
 - [62] J. L. Friedman, K. Schleich, and D. M. Witt, Topological censorship, *Phys. Rev. Lett.* **71**(1993), no. 10, 1486-1489.
 - [63] G. J. Galloway, On the topology of the domain of outer communication, *Classical Quantum Gravity* **12** (1995), no. 10, L99-L101.
 - [64] X. X. Zeng, H. Q. Zhang and H. Zhang, Shadows and photon spheres with spherical accretions in the four-dimensional Gauss–Bonnet black hole, *Eur. Phys. J. C* **80**, no.9, 872 (2020).
 - [65] J. P. Luminet, Image of a spherical black hole with thin accretion disk, *Astron. Astrophys.* **75**, 228-235 (1979).
 - [66] E. Teo, Spherical orbits around a Kerr black hole, *Gen. Rel. Grav.* **53**, no.1, 10 (2021).
 - [67] S. E. Gralla, D. E. Holz and R. M. Wald, Black Hole Shadows, Photon Rings, and Lensing Rings, *Phys. Rev. D* **100**, no. 2, 024018 (2019).
 - [68] M. Jaroszynski and A. Kurpiewski, Optics near kerr black holes: spectra of advection dominated accretion flows, *Astron. Astrophys.* **326**, 419 (1997).
 - [69] C. Bambi, Can the supermassive objects at the centers of galaxies be traversable wormholes? The first test of strong gravity for mm/sub-mm very long baseline interferometry facilities, *Phys. Rev. D* **87**, 107501 (2013).